Supplemental Materials

Molecular Biology of the Cell

Castle et al.

SUPPLEMENTAL TABLES

Table S1. Summary of published MTA results in live cells

Microtubule-binding Agent	Concentration Range (nM)	Cell Line	Growth Rate	Shortening Rate	Pause	Dynamicity	Reference
Colchicine Binding Domain (Disassembly-promoters)							
2-Methoxyestradiol	1200	MCF7	-	ns	+	-	(Kamath *et al.*, 2006)
Benomyl	3,000-5,000	MCF7	-	-	+	-	(Rathinasamy and Panda, 2008)
Carbendazim	5,000-30,000	MCF7	-	-	+	-	(Yenjerla *et al.*, 2009)
Colcemid	0.01-50	CHO	-	-	+	-	(Yang *et al.*, 2010)
Diaminothiazole	80-1600	LLC-PK1	-	-	+	-	(Thomas *et al.*, 2014)
Indanocine	2-5	MDA-MB-231	-	-	+	-	(Kapoor and Panda, 2012)
Nocodazole	50-200	NRK	-	-	+	-	(Mikhailov and Gundersen, 1998)
Nocodazole	4-400	Newt Lung	-	-	+	-	(Vasquez *et al.*, 1997)
Nocodazole	4-500	BSC-1	-	-	+	-	(Vasquez *et al.*, 1997)
TN16	25-50	MCF7	-	-	+	-	(Rai *et al.*, 2015)
Taxane Binding Domain (Assembly-promoters)							
Cabazitaxel	2	MCF7	-	-	+	-	(Azarenko *et al.*, 2014b)
Discodermolide	7-83	A549	-	-	+	-	(Honore *et al.*, 2003)
Docetaxel	2	MCF7	-	-	+	-	(Azarenko *et al.*, 2014b)
Docetaxel	0.3-3	HUVECs	ns	-	ns	-	(Kamath *et al.*, 2014)
Epothilone B	5.1	MCF7	-	-	+	-	(Chan *et al.*, 2011)
Epothilone B	0.2-3.5	MCF7	-	-	+	-	(Kamath and Jordan, 2003)
Epothilone B	1-10	U87MG	-	-	+	-	(Pagano *et al.*, 2012)
Paclitaxel	100-500	HeLa	-	-	+	-	(Jordan *et al.*, 1993)
Paclitaxel	50-100	NRK	-	-	+	-	(Mikhailov and Gundersen, 1998)
Paclitaxel	0.1-100	HMEC-1	+/ns	+/-	-/+	+/-	(Pasquier *et al.*, 2005)
Paclitaxel	0.1-100	HUVECs	+/ns	+/-	-/+	+/-	(Pasquier *et al.*, 2005)
Paclitaxel	0.1-2	A549	-	-	+	-	(Pasquier *et al.*, 2005)
Paclitaxel	100	A-498	-	-	+	-	(Yvon *et al.*, 1999)
Paclitaxel	30	Caov-C	-	-	ns	-	(Yvon *et al.*, 1999)
Paclitaxel	1.6-20	NCI-H460	-	-	+	-	(Gan *et al.*, 2010)
Paclitaxel	1-3	HUVECs	ns	-	+	-	(Kamath *et al.*, 2014)
Paclitaxel	50-150	MCF7	-	-	+	-	(Risinger *et al.*, 2014)
Paclitaxel	7.5	MCF7	-	-	nd	-	(Jordan and Kamath, 2007)
Paclitaxel	1-50	CHO	-	-	+	-	(Ganguly *et al.*, 2010)
Vinca Binding Domain (Disassembly-promoters)							
BCFMT	10,000	MCF7	-	-	+	-	(Rai *et al.*, 2012)
Eribulin	1	MCF7	-	ns	ns	-	(Jordan *et al.*, 2005)
Vinblastine	8-64	BSC-1	+/-	-	+	-	(Dhamodharan *et al.*, 1995)
Vinblastine	3-7.5	HeLa	-	nd	nd	nd	(Mohan *et al.*, 2013)
Vinblastine	0.05-15	CHO	-	-	+	-	(Yang *et al.*, 2010)
Vinblastine	1	MCF7	-	-	nd	-	(Jordan and Kamath, 2007)
Vincristine	2-40	NCI-H460	-	-	+	-	(Gan *et al.*, 2010)
Vinflunine	50	SK-N-SH	-	-	ns	-	(Pourroy *et al.*, 2004)
Vinflunine	0.1-20	HMEC-1	+/-	+/-	-/+	+/-	(Pourroy *et al.*, 2006)
Vinflunine	15	MCF7	-	ns	nd	-	(Jordan and Kamath, 2007)
Other							
Curcumin	5,000-12,000	MCF7	-	-	+	-	(Banerjee *et al.*, 2010)
Erucin	5,000-15,000	MCF7	-	-	+	-	(Azarenko *et al.*, 2014a)
Estramustine	2,000-5,000	MCF7	-	-	+	-	(Mohan and Panda, 2008)
Noscapine	25,000-250,000	PtK2	-	-	+	-	(Landen *et al.*, 2002)
Peloruside A	3.8-100	MCF7	-	-	+	-	(Chan *et al.*, 2011)
Taccalonolide AJ	25-100	MCF7	-	-	+	-	(Risinger *et al.*, 2014)

ns = not statistically significant, nd = not determined, (/) = lower conc./higher conc.
+ increased value, - decreased value

Table S2. Recovery of tubulin fluorescence after photobleaching

Condition	[*Tub*] Fraction	Fold Change	Polymer Fraction	Fold Change	p-value to Control
Control	0.20 ± 0.01	-	0.80 ± 0.01	-	-
10nM pac	0.13 ± 0.01	0.65	0.87 ± 0.01	1.09	0.058
100nM pac	0.11 ± 0.01	0.55	0.89 ± 0.01	1.11	0.018
10nM vin	0.39 ± 0.01	1.95	0.61 ± 0.01	0.76	1.5×10^{-8}
100nM vin	0.60 ± 0.03	3.02	0.40 ± 0.03	0.50	1×10^{-8}

Table S3. *In vitro* simulation base parameters for dynamic instability

Symbol	Parameter	Value	Reference
ΔG^0_{lat}	Lateral bond free energy	-5.7 k_BT	(VanBuren *et al.*, 2002, 2005; Gardner *et al.*, 2011; Coombes *et al.*, 2013)
ΔG^0_{long}	Longitudinal bond free energy	-7.2 k_BT	(Gardner *et al.*, 2011; Coombes *et al.*, 2013)
$\Delta\Delta G^0$	Energetic penalty of GDP-tubulin	+3.3 k_BT	Model fit; (VanBuren *et al.*, 2002)
[*Tub*]	Free tubulin concentration	5.6 μM	(Schek *et al.*, 2007; Gardner *et al.*, 2011)
$k_{on,PF}$	On-rate constant	6 $s^{-1}\mu M^{-1}PF^{-1}$	(Gardner *et al.*, 2011)
k_{hyd}	Hydrolysis rate constant	0.2 s^{-1}	Model constrained; (Coombes *et al.*, 2013)
σ_1	One-neighbor on-rate penalty	2	(Castle and Odde, 2013)
σ_2	Two-neighbor on-rate penalty	10	(Castle and Odde, 2013)

Table S4. *In vivo* simulation base parameters for dynamic instability

Symbol	Parameter	Value	Reference
ΔG^0_{lat}	Lateral bond free energy	-5.0 k_BT	Fit to experimental data
ΔG^0_{long}	Longitudinal bond free energy	-8.0 k_BT	Fit to experimental data
$\Delta\Delta G^0$	Energetic penalty of GDP-tubulin	+3.6 k_BT	Model fit; (VanBuren *et al.*, 2002)
[*Tub*]	Free tubulin concentration	7 μM	(Seetapun *et al.*, 2012)
$k_{on,PF}$	On-rate constant	30 $s^{-1}\mu M^{-1}PF^{-1}$	Fit to experimental data
k_{hyd}	Hydrolysis rate constant	0.8 s^{-1}	Figure 2F
σ_1	One-neighbor on-rate penalty	2	(Castle and Odde, 2013)
σ_2	Two-neighbor on-rate penalty	10	(Castle and Odde, 2013)
D_k	Kinesin motor diffusion coefficient	0.38 $\mu m^2 s^{-1}$	(Helenius *et al.*, 2006; Coombes *et al.*, 2013)
[*Kin*]	Motor concentration	5 nM	
$k_{on,k}$	Kinesin on-rate constant	0.6 $\mu m^{-1} nM^{-1} s^{-1}$	(Helenius *et al.*, 2006)
$k_{off,k}$	Kinesin off-rate	2 s^{-1}	(Helenius *et al.*, 2006)
x_{cell}	Cell membrane mean position	10 μm	Experimental data
κ_{cell}	Cell membrane stiffness	500 pN/μm	(Tinevez *et al.*, 2009)

Table S5. *In vitro* growth rate versus free tubulin concentration

Condition	Slope (nm s^{-1} μM^{-1})	Comparison to Control	Fold Decrease from Control
Control	1.46 ± 0.07	-	1.0
10nM pac	1.16 ± 0.10	p = 0.056	1.26
100nM pac	1.03 ± 0.13	p = 0.017	1.42
500nM vin	0.48 ± 0.06	$p = 4 \times 10^{-9}$	3.04

SUPPLEMENTAL FIGURE LEGENDS

Figure S1. Attenuation of microtubule dynamics by paclitaxel and vinblastine, related to Figure 1 and 2. Example kymographs from LLC-PK1 cells stably expressing EGFP-α-tubulin (A) or EB1-EGFP (B). All kymographs are on the same scale. (C) Estimated dynamic instability parameters in the presence of paclitaxel and vinblastine *in vivo*. In each plot, control values are shown in black, while paclitaxel and vinblastine are shown in cyan and magenta, respectively (light = 10 nM and dark = 100 nM). In vivo data collected at 1s intervals (n>35 microtubules from >10 cells in each condition). N.D. = not determined due to the absence of detectable growth or shortening events. All error bars are mean ± SEM. * p<0.05, ** p<0.01 compared to control. D) Maximum intensity projections of 20 s time lapse of EB1-EGFP expressing LLC-PK1 cells treated with DMSO (control, top), 100 nM paclitaxel (middle), or 10 nM vinblastine (bottom). Regions within white squares are magnified to the right. (E) Representative images of LLC-PK1α cells treated with 1 μM paclitaxel (top) or 1 μM vinblastine (bottom).

Figure S2. *In vitro* model makes similar predictions to the in vivo model with regards to dynamic instability and kinetic stabilization, related to Figure 4. (A) *In vitro* model net assembly rate for varying lateral (ΔG^0_{lat}) and longitudinal (ΔG^0_{long}) bond free energy ($k_{on,PF}$ = 6 $\mu M^{-1}s^{-1}PF^{-1}$ and [*Tub*] = 5.6 μM; contours best-fit by a polynomial), similar to that shown for the *in vivo* parameter set in Figure 3B. Cyan, red, and black circles denote the reference points for GTP, GDP, and $\Delta G^0_{tot}(v = 0)$, respectively. (B) Representative microtubule length versus time traces for the *in vitro* dynamic instability parameters listed in Table S3. Similar plots for experimental data can be found in Figure S3A. (C) The net-rate of microtubule assembly as a function of bond stabilization of both GTP- and GDP-tubulin ($\Delta\Delta G^0$ is maintained) with concurrent changes in the on-rate. All kinetic rate values were normalized to the base case for *in vitro* dynamic instability (Table S3). (D) Microtubule net-rate as a function of decreasing energetic difference between GTP- and GDP-tubulin ($\Delta\Delta G^0$) with concurrent change of the on-rate for an assembly-promoter. (E) Microtubule net-rate as a function of decreasing energetic difference between GTP- and GDP-tubulin ($\Delta\Delta G^0$) with concurrent change in the on-rate for a disassembly-promoter. In C-E, the bold boxes indicate points where dynamic instability was observed. All kinetic rate values were normalized to the base case for *in vitro* dynamic instability (Table S3). The rate reported for points of dynamic instability is the average growth rate.

Figure S3. Comparison of model predictions associated with the mechanisms of kinetic stabilization. (A) Figures 4B and D from the main text are shown. Implementing system-wide parameter changes initially identified the model-predicted mechanisms of kinetic stabilization. Estimating drug effects by this type of sensitivity analysis effectively assumes that tubulin subunits are completely saturated with the drug. Therefore, we performed additional simulations that incorporated drug on-off kinetics (see Methods), shown in B. (B) Similar plots to those shown in A, where drug kinetics are now accounted for. Here the kinetics and thermodynamics of tubulin subunits where the drug was bound were adjusted according to the values along each axis. Based on our experimental observations shown in Figure 1F, we assumed that [*drug*] = 10*K_D in all simulations shown in B, which resulted in approximately 91% saturation of tubulin subunits. Similar predictions are observed in each case: comparable parameter changes lead to kinetic stabilization in each case and observed trends regarding net-rates are observed, i.e. true kinetic stabilization desensitizes the growth rate to changes in [*Tub*] compared to pseudo-kinetic stabilization (as shown in Figure 5 of the main text). The region of pseudo-kinetic stabilization is diminished in the case where drug kinetics are simulated (B, lower). However, there remains a transition between positive and negative net-rates within this region, such that if the y-axis were sampled in a finer manner the net-rate could eventually be dialed into zero. Experimentally this would be accomplished by tubulin mass conservation (Figure 2A-C in the main text).

Figure S4. Example microtubule length traces across a range of tubulin concentrations *in vitro*, related to Figure 5. (A) Control, (B) 100 nM paclitaxel, and (C) 500 nM vinblastine. Individual tubulin concentrations are indicated, in each case concentration increases from left to right.

Figure S5. Model predictions for kinetic stabilization and the observation of dynamic instability generally, related to Figures 3, 4, and 6. (A-B) Model-predicted net rate (A) and assembly variance (B) as a function of varying $k^*_{on,PF}$ and $k_{off,PF}$ in the case where the stabilizing effect on $k_{off,PF}$ is implemented through the

longitudinal bond. (A) and (B) are identical to Figure 6C and are reproduced here for the purpose of comparison. (C-D) Model-predicted net rate (C) and assembly variance (D) as a function of varying $k^*_{on,PF}$ and $k_{off,PF}$ in the case where the stabilizing effect on $k_{off,PF}$ is implemented through the lateral bond. All kinetic rate values were normalized to the base case for *in vitro* dynamic instability (Table S3). (E) Dynamic instability in the *in vitro* model. Lateral and longitudinal bond energies, ΔG^0_{lat} and ΔG^0_{long}, were varied from -4 to -10 k_BT while all other parameters were held constant, unless indicated. Open circles denote the GTP-tubulin reference state (GDP-tubulin lateral bond is shifted by $\Delta\Delta G^0$) for individual simulations where dynamic instability was observed. Colors for different hydrolysis rates used in the simulation where black, red, and green represent k_{hyd} = 0.2, 0.4, and 1.0s^{-1}, respectively. Colored regions are a general fit to where dynamic instability was observed for each value of k_{hyd}. Dashed black line is the v = 0 nm/s contour from Figure S2A. Dashed gray line is the same contour offset by $\Delta\Delta G^0$ to indicate the initial constraints placed on the location for the GTP-tubulin reference state for the observation of dynamic instability. (F) Dynamic instability in the *in vivo* model. Again ΔG^0_{lat} and ΔG^0_{long}, were varied from -4 to -10 k_BT while all other parameters (shown in Table S4) were held constant. Dots indicate sample points where dynamic instability was observed, while the color indicates the observed rate during periods of growth. Dashed black line is the v = 0 nm/s contour from Figure 3B. Dashed gray line is the same contour offset by $\Delta\Delta G^0$ to indicate the initial constraints placed on the location for the GTP-tubulin reference state in the in vivo model. Shaded region is that constrained is approximate fit to the points where dynamic instability was observed. Because the GTP-tubulin state undergoes net assembly, its value of ΔG^0_{tot} must be more negative than the value required for net assembly (ΔG^0_{tot}; v = 0 nm/s contour from Figures 3B and S2A). Second, for the GDP-tubulin state to disassemble, the GTP value of ΔG^0_{lat} must be within $+\Delta\Delta G^0$ of the v = 0 contour (A and B). If it is further away, then the value of $\Delta\Delta G^0$ will not permit switching to a state of net disassembly, but rather two states that grow at different rates. Thus the reference GTP-tubulin point for dynamic instability is constrained to a region of parameter space with a slope of negative one and width of $\Delta\Delta G^0$. Because the observation of dynamic instability is constrained, small changes in either ΔG^0_{lat} or ΔG^0_{long} (<1k_BT *in vitro* and ~1.5 k_BT *in vivo*) are sufficient to eliminate it. In the region of more negative ΔG^0_{tot} (lower left), the microtubule grows continuously without catastrophe. Here, the GTP cap is too large for stochastic fluctuations in cap size to result in catastrophe. In the region of more positive ΔG^0_{tot} (upper right), the microtubule is unable to maintain a GTP cap and therefore cannot grow. Similarly, only small perturbations in k_{hyd} (±0.2 s^{-1}) are necessary to eliminate dynamic instability at a given point in the 2D parameter space shown in A. In the limit as k_{hyd} approaches 0 s^{-1}, dynamic instability is lost as the microtubule becomes a single-state polymer that is constantly in the GTP-tubulin state. Additionally, k_{hyd} >= 2 s^{-1} was sufficient to eliminate dynamic instability altogether because the resulting GTP cap was too small to maintain growth for any state within the constraints placed by the v = 0 contour and the value of $\Delta\Delta G^0$. Where dynamic instability was observed in the *in vivo* parameter set, microtubules with more negative ΔG^0_{long} (B, lower right) exhibited a higher growth rate compared to those with more negative ΔG^0_{lat} (B, upper left). The constraints placed on the observation of dynamic instability by the model indicate several things. First, slightly altering either bond free energy (ΔG^0_{lat} or ΔG^0_{long}) or similarly k_{hyd} could, in principle, be a viable mechanism for MTAs to eliminate dynamic instability, as each results in the loss of ability to switch between assembly states. Second, tradeoff between lateral and longitudinal bond free energy maintains dynamic instability rather than eliminating it, thus serving a way to alter the dynamics of individual microtubules without inducing kinetic stabilization (as is the case with MAPs).

Figure S6. Additional experimental observations in the presence of paclitaxel and vinblastine, related to Figures 7 and 8. (A-B) Estimated diffusion coefficients of EGFP (A) and 2x-EGFP (B) in LLC-PK1 cells treated with either 100 nM paclitaxel (cyan) or vinblastine (magenta). Error bars are mean ± SEM. (C) Microtubule tip structures in the presence of paclitaxel and vinblastine. *In vivo* model-predicted protofilament length standard deviation for each kinetic stabilization parameter set, averaged for ten separate microtubule trajectories (left) or cumulative for all microtubules (right). Control microtubules were simulated with the parameters listed in Table S4, while each kinetic stabilization case was sampled from the ellipsoidal regions in Figure 6C-D (or equivalent for cases not shown in Figure 6). tKS = true kinetic stabilization mechanism where the stabilization is applied either through the longitudinal (long) or lateral (lat) bond. pKS = pseudo-kinetic stabilization for an assembly- or disassembly-promoter. Error bars are mean ± SEM. (D) Experimentally estimated tip structures in live cells average across individual microtubules (left) or cumulative for all microtubules (right). Tip standard deviation was estimated by

fitting a Gaussian survival function to the fluorescence intensity along the microtubule axis as previously described (Demchouk *et al.*, 2011) after subtracting out the local background fluorescence parallel to the microtubule axis. **p<0.01 by multiple comparisons test. (E) Examples of extended tip structures observed in the presence of 100nM vinblastine. Arrows denote points where the fluorescence intensity along the microtubule abruptly drops, suggestive of an abrupt change in protofilament number. These extended tapers in the presence of vinblastine were stable over the course of acquisition (20 s). Due to the binding/unbinding rate of the drug, it is unlikely that these are a direct result of vinblastine. It is possible that a subset of protofilaments have been stabilized against disassembly by membrane-bound motors such as dynein (Bicek *et al.*, 2009).

SUPPLEMENTAL MOVIE CAPTIONS

Movie S1. Control simulation output. Left, animated output of the microtubule structure is shown on the left where GTP- and GDP-tubulin subunits are represented by the same color scheme used in Figure 3A. Parameters used in the simulation are described in Table S4. Upper right, the red circle denotes the microtubule length and GTP-cap size (total number of GTP-tubulin subunits in the lattice) at the current time point, corresponding to the structure on the left. Middle right, simulated image of tubulin and EB1 fluorescence using the structures shown on the left. Images were created as previously described (Gardner *et al.*, 2010; Demchouk *et al.*, 2011; Seetapun *et al.*, 2012) using the statistics (mean and standard deviation) of the cell background fluorescence and microtubule signal, averaged across all images used in analysis of control microtubule dynamics.

Movie S2. Simulation output from parameter space which is consistent with vinblastine experimental results *in vivo*. Left, animated output of the microtubule structure using the parameters indicated by the asterisk in Figure 6C. Upper right, the red circle denotes the microtubule length and GTP-cap size (total number of GTP-tubulin subunits in the lattice) at the current time point, corresponding to the structure on the left. Middle right, simulated image of tubulin and EB1 fluorescence using the structures shown on the left. Images were created as previously described (Gardner *et al.*, 2010; Demchouk *et al.*, 2011; Seetapun *et al.*, 2012) using the statistics (mean and standard deviation) of the cell background fluorescence and microtubule signal, averaged across all images used in analysis of microtubule dynamics in the presence of either 100nM or 10nM vinblastine for the tubulin or EB1 fluorescence, respectively.

Movie S3: Simulation output from parameter space which is consistent with paclitaxel experimental results *in vivo*. Left, animated output of the microtubule structure using the parameters indicated by the asterisk in Figure 6D. Upper right, the red circle denotes the microtubule length and GTP-cap size (total number of GTP-tubulin subunits in the lattice) at the current time point, corresponding to the structure on the left. Middle right, simulated image of tubulin and EB1 fluorescence using the structures shown on the left. Images were created as previously described (Gardner *et al.*, 2010; Demchouk *et al.*, 2011; Seetapun *et al.*, 2012) using the statistics (mean and standard deviation) of the cell background fluorescence and microtubule signal, averaged across all images used in analysis of microtubule dynamics in the presence of 100nM paclitaxel.

SUPPLEMENTAL REFERENCES

Azarenko, O., Jordan, M. A., and Wilson, L. (2014a). Erucin, the major isothiocyanate in arugula (Eruca sativa), inhibits proliferation of MCF7 tumor cells by suppressing microtubule dynamics. PLoS One *9*, e100599.

Azarenko, O., Smiyun, G., Mah, J., Wilson, L., and Jordan, M. A. (2014b). Antiproliferative mechanism of action of the novel taxane cabazitaxel as compared with the parent compound docetaxel in MCF7 breast cancer cells. Mol. Cancer Ther. *13*, 2092–2103.

Banerjee, M., Singh, P., and Panda, D. (2010). Curcumin suppresses the dynamic instability of microtubules, activates the mitotic checkpoint and induces apoptosis in MCF-7 cells. FEBS J. *277*, 3437–3448.

Bicek, A. D., Tüzel, E., Demtchouk, A., Uppalapati, M., Hancock, W. O., Kroll, D. M., and Odde, D. J. (2009). Anterograde microtubule transport drives microtubule bending in LLC-PK1 epithelial cells. Mol. Biol. Cell *20*, 2943–2953.

Castle, B. T., and Odde, D. J. (2013). Brownian dynamics of subunit addition-loss kinetics and thermodynamics in linear polymer self-assembly. Biophys. J. *105*, 2528–2540.

Chan, A., Andreae, P. M., Northcote, P. T., and Miller, J. H. (2011). Peloruside A inhibits microtubule dynamics in a breast cancer cell line MCF7. Invest. New Drugs *29*, 615–626.

Coombes, C. E., Yamamoto, A., Kenzie, M. R., Odde, D. J., and Gardner, M. K. (2013). Evolving Tip Structures Can Explain Age-Dependent Microtubule Catastrophe. Curr. Biol. *23*, 1342–1348.

Demchouk, A. O., Gardner, M. K., and Odde, D. J. (2011). Microtubule Tip Tracking and Tip Structures at the Nanometer Scale Using Digital Fluorescence Microscopy. Cell. Mol. Bioeng. *4*, 192–204.

Dhamodharan, R., Jordan, M. A., Thrower, D., Wilson, L., and Wadsworth, P. (1995). Vinblastine suppresses dynamics of individual microtubules in living interphase cells. Mol. Biol. Cell *6*, 1215–1229.

Gan, P. P., McCarroll, J. A., Po'uha, S. T., Kamath, K., Jordan, M. A., and Kavallaris, M. (2010). Microtubule dynamics, mitotic arrest, and apoptosis: drug-induced differential effects of betaIII-tubulin. Mol. Cancer Ther. *9*, 1339–1348.

Ganguly, A., Yang, H., and Cabral, F. (2010). Paclitaxel-dependent cell lines reveal a novel drug activity. Mol. Cancer Ther. *9*, 2914–2923.

Gardner, M. K., Charlebois, B. D., Jánosi, I. M., Howard, J., Hunt, A. J., and Odde, D. J. (2011). Rapid microtubule self-assembly kinetics. Cell *146*, 582–592.

Gardner, M. K., Sprague, B. L., Pearson, C. G., Cosgrove, B. D., Bicek, A. D., Bloom, K., Salmon, E. D., and Odde, D. J. (2010). Model Convolution: A Computational Approach to Digital Image Interpretation. Cell. Mol. Bioeng. *3*, 163–170.

Helenius, J., Brouhard, G., Kalaidzidis, Y., Diez, S., and Howard, J. (2006). The depolymerizing kinesin MCAK uses lattice diffusion to rapidly target microtubule ends. Nature *441*, 115–119.

Honore, S., Kamath, K., Braguer, D., Wilson, L., Briand, C., and Jordan, M. A. (2003). Suppression of microtubule dynamics by discodermolide by a novel mechanism is associated with mitotic arrest and inhibition of tumor cell proliferation. Mol. Cancer Ther. *2*, 1303–1311.

Jordan, M. A., and Kamath, K. (2007). How do microtubule-targeted drugs work? An overview. Curr. Cancer Drug Targets *7*, 730–742.

Jordan, M. A., Kamath, K., Manna, T., Okouneva, T., Miller, H. P., Davis, C., Littlefield, B. A., and Wilson, L. (2005). The primary antimitotic mechanism of action of the synthetic halichondrin E7389 is suppression of microtubule growth. Mol. Cancer Ther. *4*, 1086–1095.

Jordan, M. A., Toso, R. J., Thrower, D., and Wilson, L. (1993). Mechanism of mitotic block and inhibition of cell proliferation by taxol at low concentrations. Proc. Natl. Acad. Sci. U. S. A. *90*, 9552–9556.

Kamath, K., and Jordan, M. A. (2003). Suppression of microtubule dynamics by epothilone B is associated with mitotic arrest. Cancer Res. *63*, 6026–6031.

Kamath, K., Okouneva, T., Larson, G., Panda, D., Wilson, L., and Jordan, M. A. (2006). 2-Methoxyestradiol suppresses microtubule dynamics and arrests mitosis without depolymerizing microtubules. Mol. Cancer Ther. *5*, 2225–2233.

Kamath, K., Smiyun, G., Wilson, L., and Jordan, M. A. (2014). Mechanisms of inhibition of endothelial cell migration by taxanes. Cytoskeleton (Hoboken). *71*, 46–60.

Kapoor, S., and Panda, D. (2012). Kinetic stabilization of microtubule dynamics by indanocine perturbs EB1

localization, induces defects in cell polarity and inhibits migration of MDA-MB-231 cells. Biochem. Pharmacol. *83*, 1495–1506.

Landen, J. W. *et al.* (2002). Noscapine alters microtubule dynamics in living cells and inhibits the progression of melanoma. Cancer Res. *62*, 4109–4114.

Mikhailov, A., and Gundersen, G. G. (1998). Relationship between microtubule dynamics and lamellipodium formation revealed by direct imaging of microtubules in cells treated with nocodazole or taxol. Cell Motil. Cytoskeleton *41*, 325–340.

Mohan, R., Katrukha, E. A., Doodhi, H., Smal, I., Meijering, E., Kapitein, L. C., Steinmetz, M. O., and Akhmanova, A. (2013). End-binding proteins sensitize microtubules to the action of microtubule-targeting agents. Proc. Natl. Acad. Sci. U. S. A. *110*, 8900–8905.

Mohan, R., and Panda, D. (2008). Kinetic stabilization of microtubule dynamics by estramustine is associated with tubulin acetylation, spindle abnormalities, and mitotic arrest. Cancer Res. *68*, 6181–6189.

Pagano, A., Honoré, S., Mohan, R., Berges, R., Akhmanova, A., and Braguer, D. (2012). Epothilone B inhibits migration of glioblastoma cells by inducing microtubule catastrophes and affecting EB1 accumulation at microtubule plus ends. Biochem. Pharmacol. *84*, 432–443.

Pasquier, E., Honore, S., Pourroy, B., Jordan, M. A., Lehmann, M., Briand, C., and Braguer, D. (2005). Antiangiogenic concentrations of paclitaxel induce an increase in microtubule dynamics in endothelial cells but not in cancer cells. Cancer Res. *65*, 2433–2440.

Pourroy, B., Carre, M., Honore, S., Bourgarel-Rey, V., Kruczynski, A., Briand, C., and Braguer, D. (2004). Low Concentrations of Vinflunine Induce Apoptosis in Human SK-N-SH Neuroblastoma Cells through a Postmitotic G1 Arrest and a Mitochondrial Pathway. Mol. Pharmacol. *66*, 580–591.

Pourroy, B., Honoré, S., Pasquier, E., Bourgarel-Rey, V., Kruczynski, A., Briand, C., and Braguer, D. (2006). Antiangiogenic concentrations of vinflunine increase the interphase microtubule dynamics and decrease the motility of endothelial cells. Cancer Res. *66*, 3256–3263.

Rai, A., Kapoor, S., Singh, S., Chatterji, B. P., and Panda, D. (2015). Transcription factor NF-κB associates with microtubules and stimulates apoptosis in response to suppression of microtubule dynamics in MCF-7 cells. Biochem. Pharmacol. *93*, 277–289.

Rai, A., Surolia, A., and Panda, D. (2012). An antitubulin agent BCFMT inhibits proliferation of cancer cells and induces cell death by inhibiting microtubule dynamics. PLoS One *7*, e44311.

Rathinasamy, K., and Panda, D. (2008). Kinetic stabilization of microtubule dynamic instability by benomyl increases the nuclear transport of p53. Biochem. Pharmacol. *76*, 1669–1680.

Risinger, A. L., Riffle, S. M., Lopus, M., Jordan, M. A., Wilson, L., and Mooberry, S. L. (2014). The taccalonolides and paclitaxel cause distinct effects on microtubule dynamics and aster formation. Mol. Cancer *13*, 41.

Schek, H. T., Gardner, M. K., Cheng, J., Odde, D. J., and Hunt, A. J. (2007). Microtubule assembly dynamics at the nanoscale. Curr. Biol. *17*, 1445–1455.

Seetapun, D., Castle, B. T., McIntyre, A. J., Tran, P. T., and Odde, D. J. (2012). Estimating the microtubule GTP cap size in vivo. Curr. Biol. *22*, 1681–1687.

Thomas, N. E., Thamkachy, R., Sivakumar, K. C., Sreedevi, K. J., Louis, X. L., Thomas, S. A., Kumar, R., Rajasekharan, K. N., Cassimeris, L., and Sengupta, S. (2014). Reversible action of diaminothiazoles in cancer cells is implicated by the induction of a fast conformational change of tubulin and suppression of microtubule dynamics. Mol. Cancer Ther. *13*, 179–189.

Tinevez, J.-Y., Schulze, U., Salbreux, G., Roensch, J., Joanny, J.-F., and Paluch, E. (2009). Role of cortical tension in bleb growth. Proc. Natl. Acad. Sci. U. S. A. *106*, 18581–18586.

VanBuren, V., Cassimeris, L., and Odde, D. J. (2005). Mechanochemical model of microtubule structure and self-assembly kinetics. Biophys. J. *89*, 2911–2926.

VanBuren, V., Odde, D. J., and Cassimeris, L. (2002). Estimates of lateral and longitudinal bond energies within the microtubule lattice. Proc. Natl. Acad. Sci. U. S. A. *99*, 6035–6040.

Vasquez, R. J., Howell, B., Yvon, A. M., Wadsworth, P., and Cassimeris, L. (1997). Nanomolar concentrations of nocodazole alter microtubule dynamic instability in vivo and in vitro. Mol. Biol. Cell *8*, 973–985.

Yang, H., Ganguly, A., and Cabral, F. (2010). Inhibition of cell migration and cell division correlates with distinct effects of microtubule inhibiting drugs. J. Biol. Chem. *285*, 32242–32250.

Yenjerla, M., Cox, C., Wilson, L., and Jordan, M. A. (2009). Carbendazim inhibits cancer cell proliferation by

suppressing microtubule dynamics. J. Pharmacol. Exp. Ther. *328*, 390–398.

Yvon, A. M., Wadsworth, P., and Jordan, M. A. (1999). Taxol suppresses dynamics of individual microtubules in living human tumor cells. Mol. Biol. Cell *10*, 947–959.

Figure S1

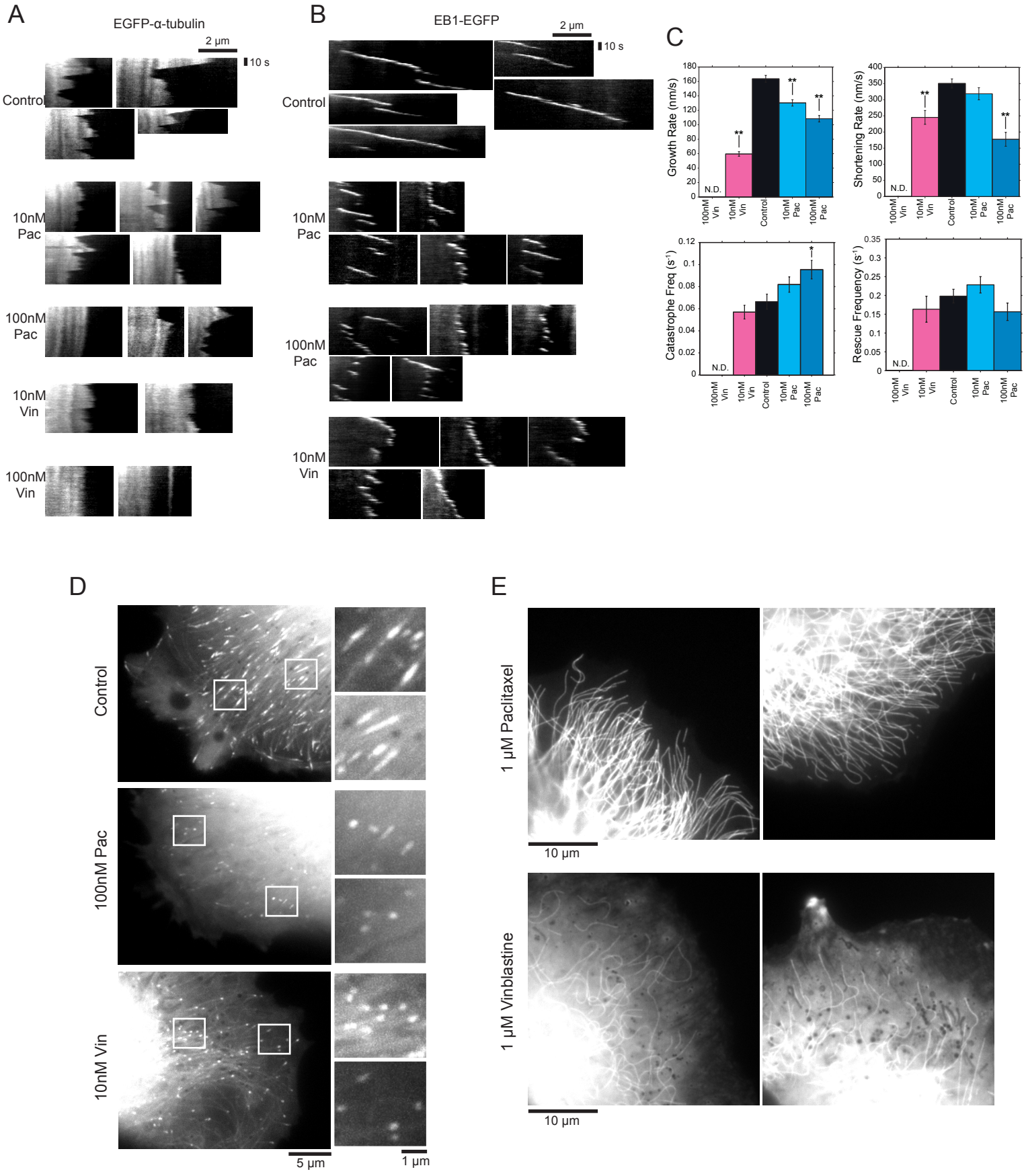
A
EGFP-α-tubulin
2 μm
10 s
Control
10nM Pac
100nM Pac
10nM Vin
100nM Vin
B
EB1-EGFP
2 μm
10 s
Control
10nM Pac
100nM Pac
10nM Vin
C
Growth Rate (nm/s)
Shortening Rate (nm/s)
Catastrophe Freq (s-1)
Rescue Frequency (s-1)
N.D.
100nM Vin
10nM Vin
Control
10nM Pac
100nM Pac
D
Control
100nM Pac
10nM Vin
5 μm
1 μm
E
1 μM Paclitaxel
1 μM Vinblastine
10 μm
10 μm

Figure S2

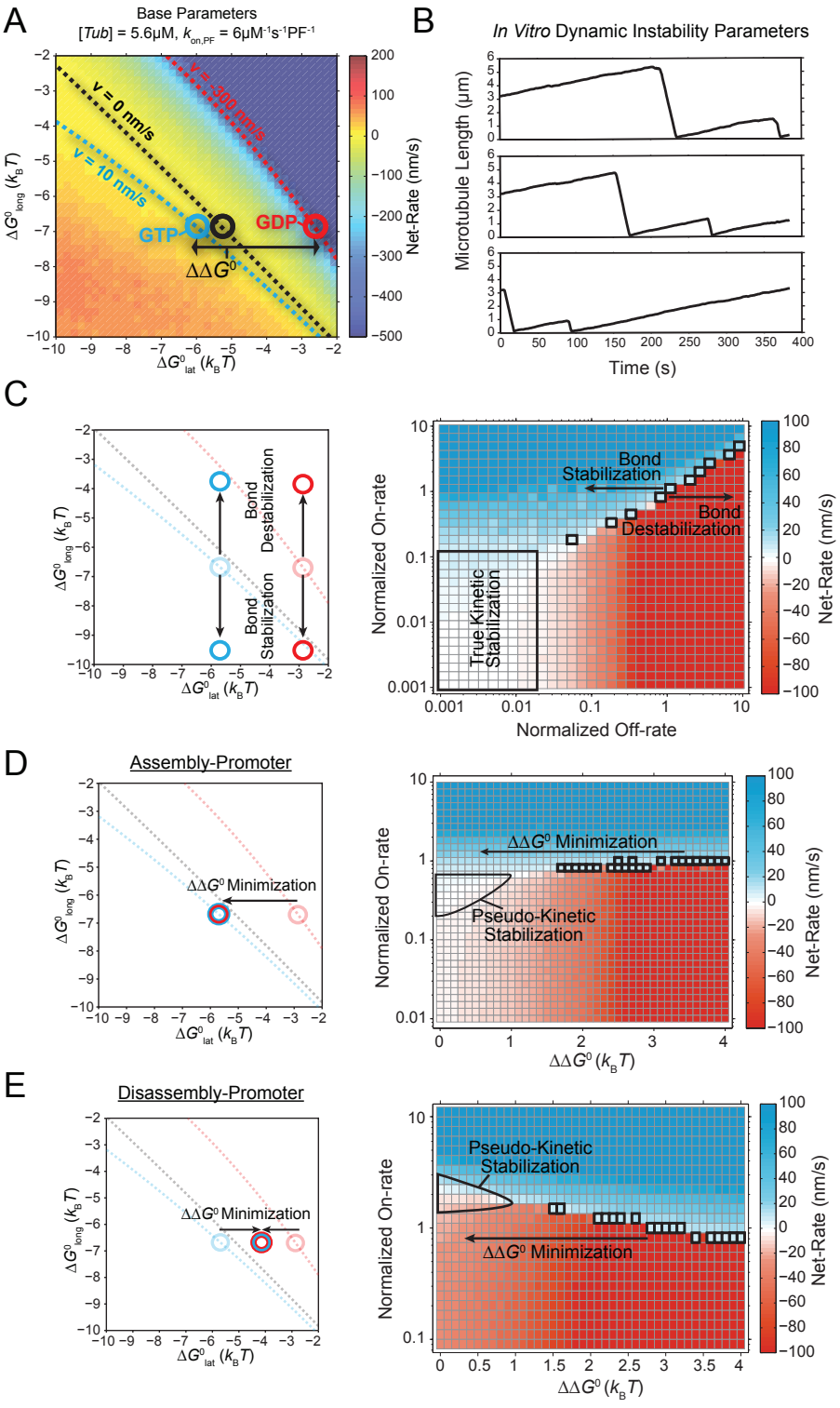
A
Base Parameters
[Tub] = 5.6μM, $k_{on,PF}$ = 6μM^{-1}s^{-1}PF^{-1}
v = 0 nm/s
v = 10 nm/s
v = 100 nm/s
GTP
GDP
ΔΔG⁰
ΔG⁰long (kBT)
ΔG⁰lat (kBT)
Net-Rate (nm/s)
B
In Vitro Dynamic Instability Parameters
Microtubule Length (μm)
Time (s)
C
Bond Destabilization
Bond Stabilization
Normalized On-rate
Normalized Off-rate
True Kinetic Stabilization
D
Assembly-Promoter
ΔΔG⁰ Minimization
Pseudo-Kinetic Stabilization
E
Disassembly-Promoter

Figure S3

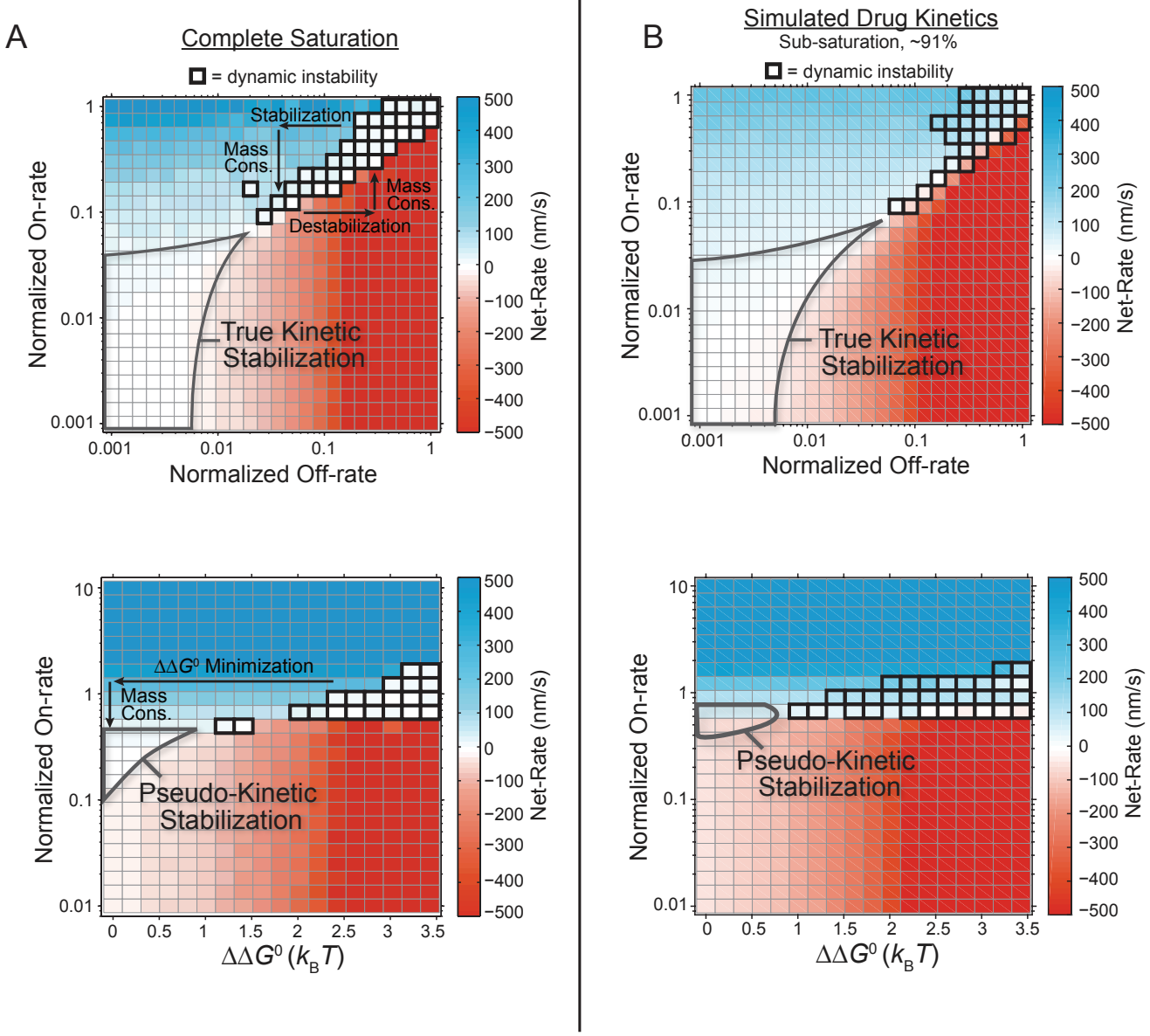
A
Complete Saturation
= dynamic instability
Stabilization
Mass Cons.
Mass Cons.
Destabilization
True Kinetic Stabilization
Normalized On-rate
Normalized Off-rate
Net-Rate (nm/s)
ΔΔG⁰ Minimization
Mass Cons.
Pseudo-Kinetic Stabilization
ΔΔG⁰ (k_B T)
B
Simulated Drug Kinetics
Sub-saturation, ~91%
= dynamic instability
True Kinetic Stabilization
Pseudo-Kinetic Stabilization

Figure S4

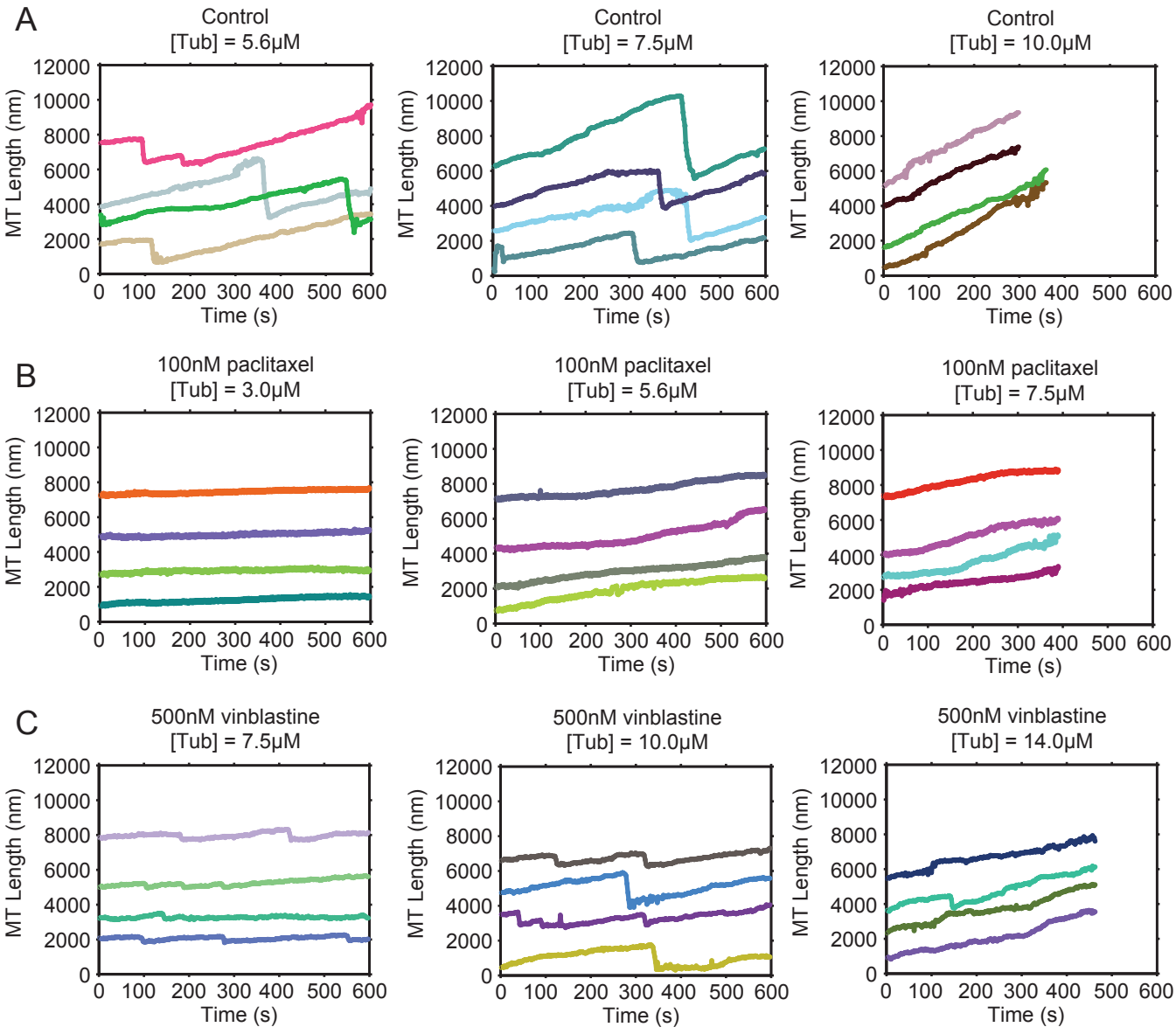
A
Control
[Tub] = 5.6μM
Control
[Tub] = 7.5μM
Control
[Tub] = 10.0μM
B
100nM paclitaxel
[Tub] = 3.0μM
100nM paclitaxel
[Tub] = 5.6μM
100nM paclitaxel
[Tub] = 7.5μM
C
500nM vinblastine
[Tub] = 7.5μM
500nM vinblastine
[Tub] = 10.0μM
500nM vinblastine
[Tub] = 14.0μM
MT Length (nm)
Time (s)
0
2000
4000
6000
8000
10000
12000
0 100 200 300 400 500 600

Figure S5

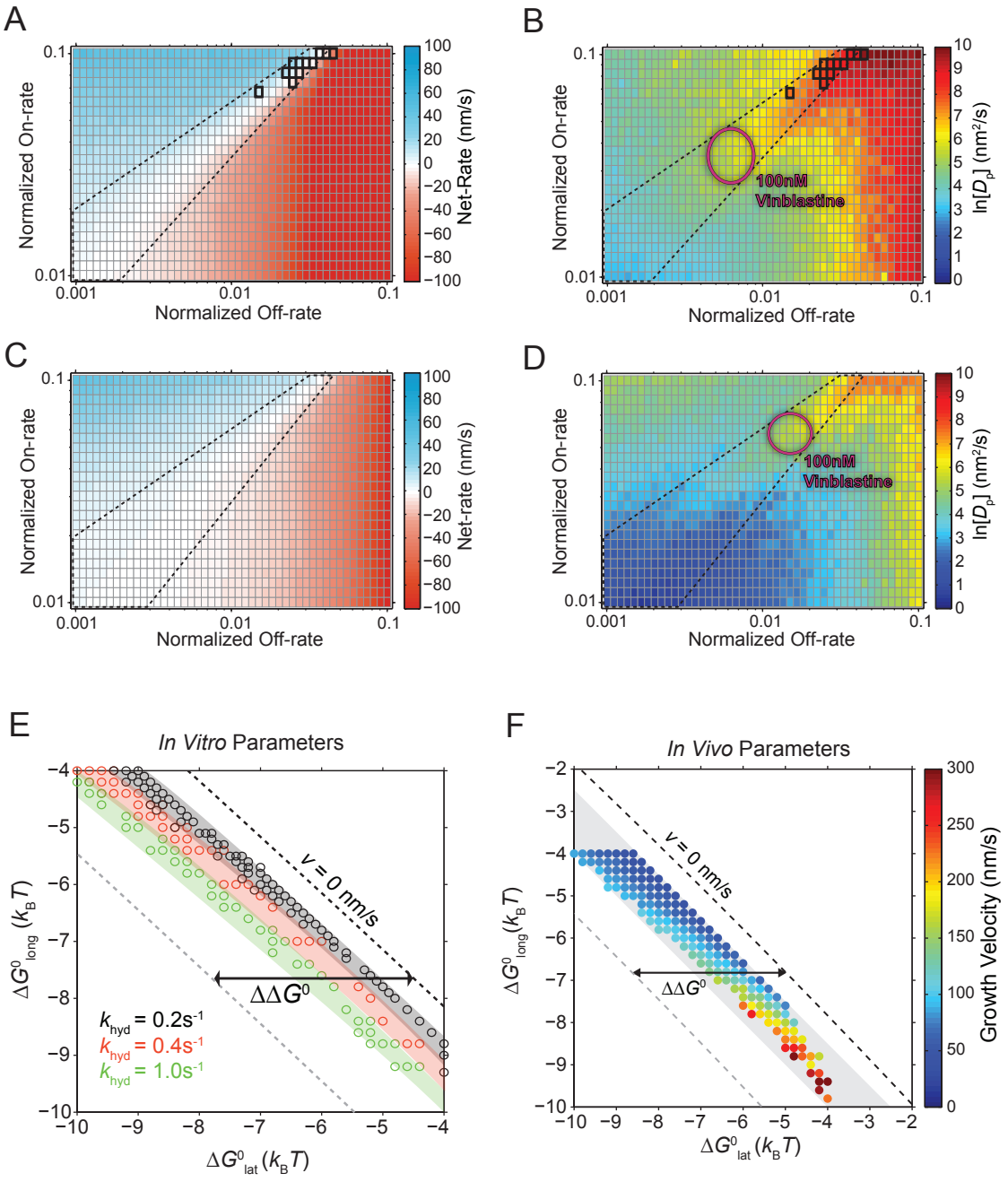
A
B
C
D
E
F
Normalized On-rate
Normalized Off-rate
Net-Rate (nm/s)
ln[D_p] (nm^2/s)
100nM
Vinblastine
In Vitro Parameters
In Vivo Parameters
$v = 0$ nm/s
$\Delta\Delta G^0$
k_{hyd} = 0.2s^{-1}
k_{hyd} = 0.4s^{-1}
k_{hyd} = 1.0s^{-1}
ΔG^0_{long} ($k_B T$)
ΔG^0_{lat} ($k_B T$)
Growth Velocity (nm/s)

Figure S6

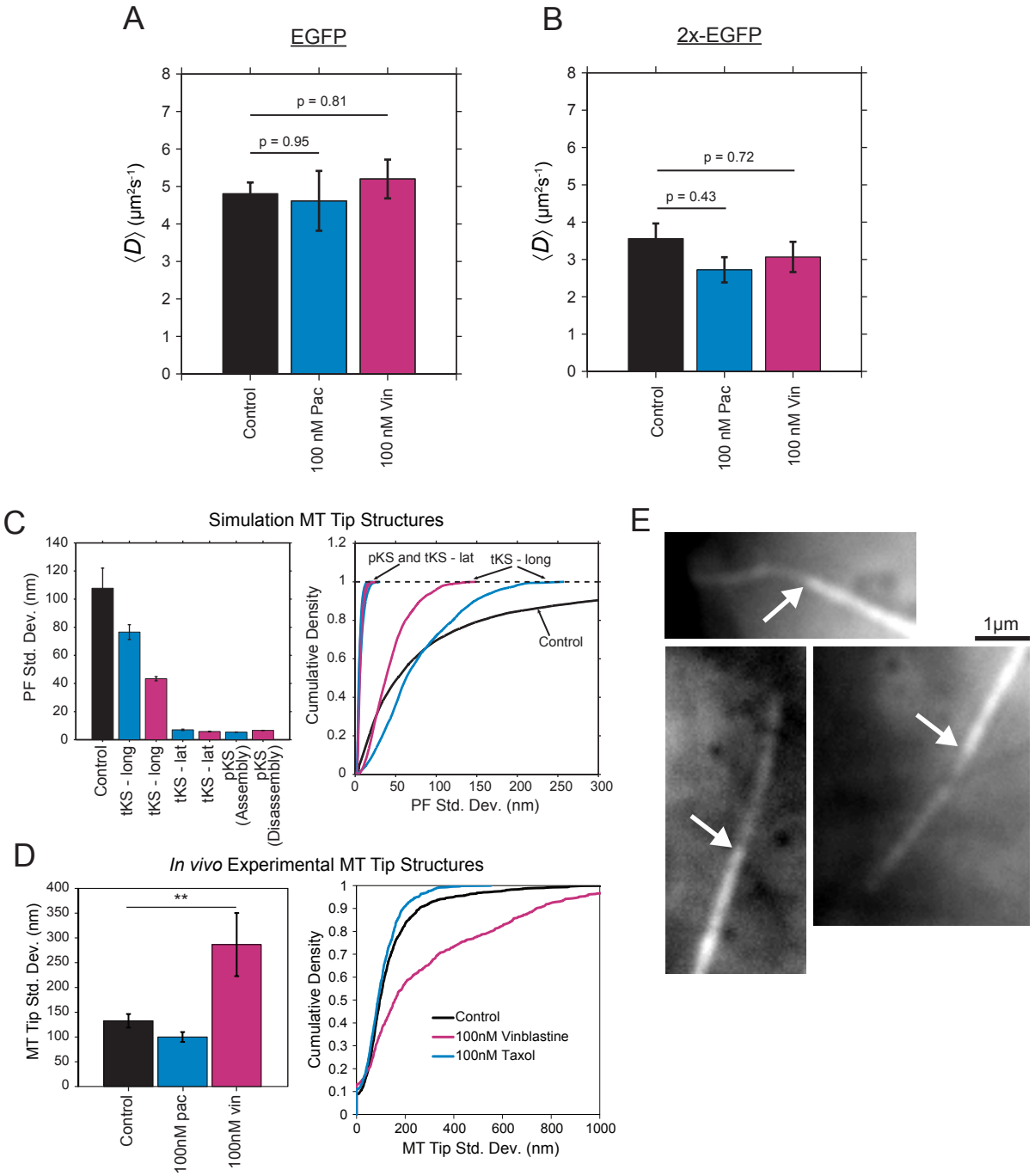
A
EGFP
p = 0.81
p = 0.95
⟨D⟩ (μm²s⁻¹)
Control
100 nM Pac
100 nM Vin
B
2x-EGFP
p = 0.72
p = 0.43
C
Simulation MT Tip Structures
PF Std. Dev. (nm)
Control
tKS - long
tKS - long
tKS - lat
tKS - lat
pKS (Assembly)
pKS (Disassembly)
Cumulative Density
pKS and tKS - lat
tKS - long
Control
PF Std. Dev. (nm)
D
In vivo Experimental MT Tip Structures
MT Tip Std. Dev. (nm)
**
Control
100nM pac
100nM vin
Cumulative Density
Control
100nM Vinblastine
100nM Taxol
MT Tip Std. Dev. (nm)
E
1μm